

Joint Constraints on Fuzzy and Warm Dark Matter from Satellite Populations of the Milky Way and Andromeda

JIANXIANG LIU ^{1,2} YAN GONG ^{1,2,3} AND KAI LIAO ⁴

¹*National Astronomical Observatories, Chinese Academy of Sciences, 20A Datun Road, Beijing 100101, China*

²*School of Astronomy and Space Sciences, University of Chinese Academy of Sciences,
No.19A Yuquan Road, Beijing 100049, China*

³*Science Center for Chinese Space Station Survey Telescope, National Astronomical Observatories,
Chinese Academy of Science, 20A Datun Road, Beijing 100101, China*

⁴*School of Physics and Technology, Wuhan University, Wuhan 430072, China*

ABSTRACT

We perform a joint analysis of the Milky Way (MW) and Andromeda (M31) satellite populations to constrain the properties of fuzzy dark matter (FDM) and thermal-relic warm dark matter (WDM). We combine MW satellite observations from the Dark Energy Survey (DES) and Pan-STARRS1 (PS1) with M31 satellite data from the Pan-Andromeda Archaeological Survey (PAndAS), and model the corresponding observable satellite populations using the galaxy–halo connection model together with the appropriate selection functions. Uncertainties in the virial masses of the MW and M31 are incorporated through host-mass priors that linearly scale the relevant model parameters, allowing us to infer the full posterior distributions of all parameters. For the FDM case, we obtain $m_{\text{FDM}} > 1.75 \times 10^{-20}$ eV (95% CL) and $m_{\text{FDM}} > 1.41 \times 10^{-20}$ eV (20:1 posterior ratio). For thermal-relic WDM, we find $m_{\text{WDM}} > 6.22$ keV (95% CL) and $m_{\text{WDM}} > 5.75$ keV (20:1 posterior ratio). These results represent a moderate improvement over MW-only constraints, and provide the strongest constraints to date on the FDM and WDM derived from satellite galaxy populations in the Local Group.

Keywords: Dark matter (353) — Milky Way dark matter halo (1049) — Andromeda Galaxy (39) — Galaxy abundances (574) — Dwarf galaxies (416) — Local Group (929)

1. INTRODUCTION

Dark matter (DM) constitutes the dominant component of matter in the Universe (Planck Collaboration et al. 2020a). Its existence is supported by multiple cosmological and astrophysical observations, such as the cosmic microwave background (CMB; Planck Collaboration et al. 2020b) and galaxy rotation curves (T. S. van Albada et al. 1985), yet its true nature remains elusive. The cold dark matter (CDM) paradigm, exemplified by weakly interacting massive particles (WIMPs), has achieved remarkable success in explaining the large-scale structure (LSS) of the Universe (G. Jungman et al. 1996; D. Nelson et al. 2018). However, it faces several well-known small-scale challenges: the missing-satellite problem, the cusp–core problem, and the too-big-to-fail problem (A. Del Popolo & M. Le Delliou 2017).

To address these issues and motivated by the lack of any experimental detection of CDM particles, several non-CDM models have been proposed or revisited, such as fuzzy dark matter (FDM; W. Hu et al. 2000; L. Hui 2021; A. Eberhardt & E. G. M. Ferreira 2025), warm dark matter (WDM; A. Boyarsky et al. 2019), and interacting dark matter (IDM; C. Boehm et al. 2001; V. Gluscevic & K. K. Boddy 2018). These non-CDM scenarios reproduce the LSS of the Universe while simultaneously altering the linear matter power spectrum and the abundance of halos and subhalos on small scales.

Dwarf galaxies, as low-mass and DM-dominated systems, serve as powerful probes of small-scale dark matter structure (D. J. E. Marsh & J. C. Niemeyer 2019; E. O. Nadler et al. 2021b; T. Zimmermann et al. 2025). Following the success of the Sloan Digital Sky Survey (SDSS) in the early 2000s (B. Willman et al. 2005a,b), an increasing number of dwarf galaxies, including progressively fainter systems, have been discovered and continue to be found (A. W. McConnachie et al. 2009;

Dark Energy Survey Collaboration et al. 2016; K. C. Chambers et al. 2016; A. W. McConnachie et al. 2018; A. Drlica-Wagner et al. 2020; A. Doliva-Dolinsky et al. 2022; H. Qu et al. 2023; K. Tsiane et al. 2025; CSST Collaboration et al. 2025; C. Y. Tan et al. 2025b), further motivating the use of dwarf galaxies to study dark matter models. Non-CDM models can suppress the abundance of halos and subhalos, and since satellite dwarf galaxies reside within subhalos, it is well-motivated to use their observed abundance to probe the underlying subhalo population, thereby placing constraints on non-CDM models (E. O. Nadler et al. 2021b; O. Newton et al. 2021; A. Dekker et al. 2022; C. Y. Tan et al. 2025a; E. O. Nadler et al. 2025).

For instance, E. O. Nadler et al. (2021b) and C. Y. Tan et al. (2025a) use the galaxy–halo connection model introduced in E. O. Nadler et al. (2020) together with observations of Milky Way (MW) satellites from the Dark Energy Survey (DES; Dark Energy Survey Collaboration et al. 2016) and Pan-STARRS1 (PS1; K. C. Chambers et al. 2016) to constrain various non-CDM models. E. O. Nadler et al. (2025) use the same modeling framework and data, incorporating updated transfer functions and subhalo mass functions to constrain FDM, WDM, and IDM. In addition, O. Newton et al. (2021) and A. Dekker et al. (2022) develop different semi-analytic frameworks and use the predicted total number of MW satellites from O. Newton et al. (2018) and E. O. Nadler et al. (2020) to place constraints on WDM.

In this paper, we present the joint constraints on non-CDM models using the satellite populations of the MW and Andromeda Galaxy (M31). Specifically, we adopt and slightly modify the galaxy–halo connection model introduced by E. O. Nadler et al. (2020) and use observations of MW satellites from DES and PS1 together with M31 satellites from the Pan-Andromeda Archaeological Survey (PAndAS; A. W. McConnachie et al. 2009, 2018; A. Doliva-Dolinsky et al. 2022, 2023) to constrain the properties of FDM and WDM. Using both satellite populations allows us to improve the overall precision of the constraints, compared to using only the MW satellite population (E. O. Nadler et al. 2024).

This paper is organized as follows: in Section 2, we introduce the FDM and WDM models considered in this work; the observational data of satellite galaxies are presented in Section 3; Section 4 describes the modeling framework; in Section 5, we show the constraint results on the FDM and WDM models; in Section 6, we discuss additional results derived from our modeling framework; we provide a summary and outlook in Section 7. Following Y.-Y. Mao et al. (2015) and E. O. Nadler et al. (2025), we adopt the cosmological param-

eters $h = 0.7$, $\Omega_m = 0.286$, $\Omega_b = 0.049$, $\Omega_\Lambda = 0.714$, $\sigma_8 = 0.82$, and $n_s = 0.96$ (G. Hinshaw et al. 2013). This choice has a negligible impact on our results. Halo masses are defined using the virial overdensity criterion of G. L. Bryan & M. L. Norman (1998), which corresponds to $\Delta_{\text{vir}} \approx 99 \rho_{\text{crit}}$ in our cosmology, where ρ_{crit} is the critical density of the Universe at $z = 0$.

2. DARK MATTER MODELS

In this section, we discuss the transfer functions and subhalo mass functions of the non-CDM models, and present the details of the FDM and WDM models we adopt in this work.

2.1. Non-cold dark matter models

For many non-CDM models, the linear matter power spectrum is identical to that of CDM on large scales but deviates on small scales. The FDM and WDM models considered in this work both can suppress small-scale power, through different physical mechanisms. To quantify their deviations from CDM, we normalize the linear matter power spectrum of each non-CDM model by that of CDM, defining the transfer function as

$$\mathcal{T}_{\text{non-CDM}}^2(k) = \frac{P_{\text{non-CDM}}(k)}{P_{\text{CDM}}(k)}, \quad (1)$$

where k is the cosmological wave number, $P_{\text{CDM}}(k)$ is the CDM linear matter power spectrum, and $P_{\text{non-CDM}}(k)$ is the linear matter power spectrum of a non-CDM model (P. Bode et al. 2001).

The transfer functions we consider represent the suppression of the linear matter power spectrum in non-CDM models relative to CDM. To quantify the strength of this suppression, we introduce the half-mode wavenumber k_{hm} , defined as the scale at which the power is reduced to one quarter of that in CDM (A. Schneider et al. 2012), which is given by

$$\mathcal{T}_{\text{non-CDM}}^2(k_{\text{hm}}) = 0.25. \quad (2)$$

In the linear theory, the halo mass and comoving wavenumber are related by (E. O. Nadler et al. 2019a)

$$M(k) \equiv \frac{4\pi}{3} \Omega_m \rho_{\text{crit}} \left(\frac{\pi}{k} \right)^3. \quad (3)$$

The half-mode mass corresponding to k_{hm} is then defined as $M_{\text{hm}} \equiv M(k_{\text{hm}})$.

The non-CDM models suppress the number of subhalos by reducing the linear matter power spectrum on small scales, and the suppression of the subhalo mass function in non-CDM models relative to CDM, $f_{\text{non-CDM}}(M)$, can be expressed as

$$\left(\frac{dN_{\text{sub}}}{dM} \right)_{\text{non-CDM}} = f_{\text{non-CDM}}(M) \left(\frac{dN_{\text{sub}}}{dM} \right)_{\text{CDM}}, \quad (4)$$

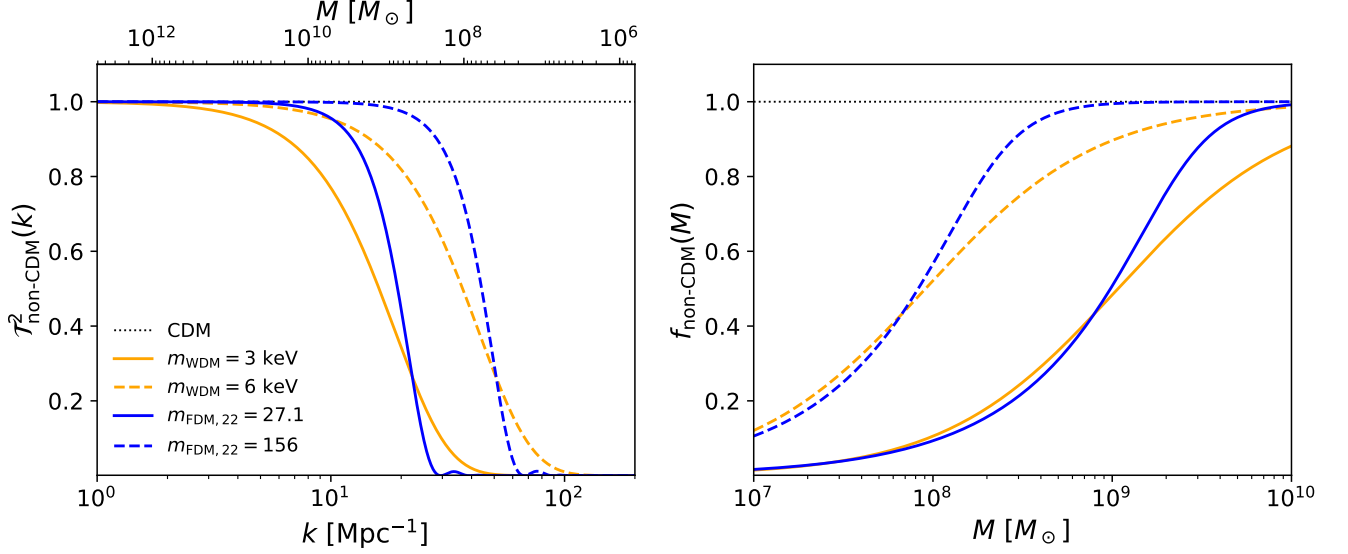


Figure 1. The left and right panels show the transfer functions and subhalo mass function suppressions for FDM (blue) and WDM (orange), respectively. In the left panel, the lower x -axis indicates the cosmological wavenumber, while the upper x -axis shows the corresponding halo mass. In the right panel, the x -axis represents the peak virial mass. Different line styles correspond to different particle masses, and models with the same line style have the same half-mode mass M_{hm} . The solid and dashed curves correspond to $M_{\text{hm}} = 4.30 \times 10^8 M_\odot$ and $3.64 \times 10^7 M_\odot$, respectively.

where M is the peak virial mass (E. O. Nadler et al. 2025). It should be noted that the specific forms of $\mathcal{T}_{\text{non-CDM}}^2(k)$ and $f_{\text{non-CDM}}(M)$ depend on the particular dark matter model and its underlying properties. Furthermore, the half-mode mass M_{hm} derived from $\mathcal{T}_{\text{non-CDM}}^2(k)$ provides a useful characteristic scale that facilitates the construction of $f_{\text{non-CDM}}(M)$.

2.2. Fuzzy dark matter

FDM consists of ultra-light bosons with mass $m_{\text{FDM}} \sim 10^{-22}$ eV, whose de Broglie wavelength is on the kiloparsec scale, comparable to the size of dwarf galaxies. Due to quantum pressure, the formation of small-scale structures is suppressed (W. Hu et al. 2000; L. Hui 2021). Following E. O. Nadler et al. (2025), we define

$$m_{\text{FDM},22} \equiv \frac{m_{\text{FDM}}}{10^{-22} \text{ eV}}. \quad (5)$$

We adopt the FDM transfer function (S. Passaglia & W. Hu 2022)

$$\mathcal{T}_{\text{FDM}}^2(k, m_{\text{FDM},22}) = \left[\frac{\sin(x^m)}{x^m(1 + Bx^{6-m})} \right]^2, \quad (6)$$

where $m = 5/2$, $x \equiv A(k/k_J)$, $k_J \equiv 9 \text{ Mpc}^{-1} \times m_{\text{FDM},22}^{1/2}$, $A = 2.22(m_{\text{FDM},22})^{1/25 - \ln(m_{\text{FDM},22})/1000}$, and $B = 0.16(m_{\text{FDM},22})^{-1/20}$. We then obtain the half-mode mass, and it can be expressed as

$$M_{\text{hm}}(m_{\text{FDM},22}) = 4.5 \times 10^{10} M_\odot \times m_{\text{FDM},22}^{-1.41}. \quad (7)$$

Using the results from E. O. Nadler et al. (2025), the suppression of the subhalo mass function in FDM relative to CDM can be written as

$$f_{\text{FDM}}(M, m_{\text{FDM},22}) = \left[1 + \left(\frac{\alpha M_{\text{hm}}(m_{\text{FDM},22})}{M} \right)^\beta \right]^{-\gamma}, \quad (8)$$

where $\alpha = 5.5$, $\beta = 2.5$ and $\gamma = 0.3$.

2.3. Warm dark matter

In this work, we consider the simplest thermal-relic WDM, whose properties are determined solely by the particle mass m_{WDM} , which is typically a few keV. The non-negligible free-streaming effect of WDM can suppress the formation of small-scale structures (A. Boyarsky et al. 2019).

Following the same procedure as for FDM, we adopt the WDM transfer function from M. Viel et al. (2005), which is given by

$$\mathcal{T}_{\text{WDM}}^2(k, m_{\text{WDM}}) = \left[1 + (\alpha(m_{\text{WDM}}) \times k)^{2\nu} \right]^{-10/\nu}, \quad (9)$$

where we take $\nu = 1.049$, and $\alpha(m_{\text{WDM}})$ can be expressed as (C. M. Vogel & K. N. Abazajian 2023)

$$\alpha(m_{\text{WDM}}) = a \left(\frac{m_{\text{WDM}}}{1 \text{ keV}} \right)^b \left(\frac{\omega_{\text{WDM}}}{0.12} \right)^\eta \left(\frac{h}{0.6736} \right)^\theta h^{-1} \text{ Mpc}, \quad (10)$$

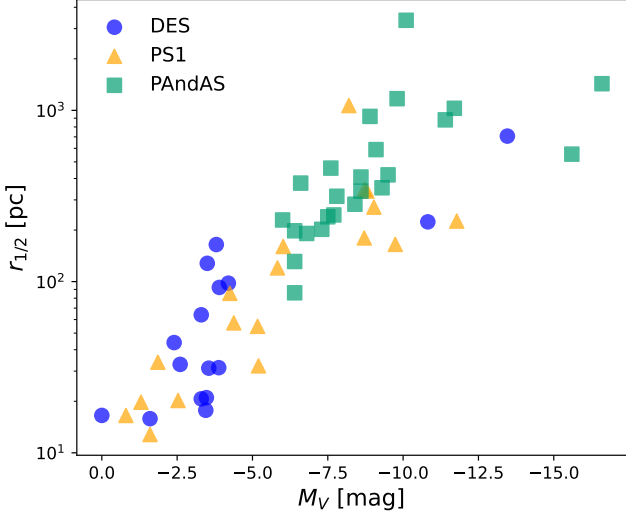


Figure 2. The half-light radii $r_{1/2}$ of the satellite galaxy data we use as a function of the absolute magnitudes M_V . The blue dots, orange triangles, and green squares mark the satellites from the DES, PS1, and PAndAS, respectively.

where $a = 0.0437$, $b = -1.188$, $\eta = 0.2463$, $\theta = 2.012$, and $\omega_{\text{WDM}} \equiv \Omega_{\text{WDM}} h^2$. Then we can get the half-mode mass

$$M_{\text{hm}}(m_{\text{WDM}}) = 4.3 \times 10^8 M_{\odot} \times \left(\frac{m_{\text{WDM}}}{3 \text{ keV}} \right)^{-3.564}. \quad (11)$$

Similarly, using the results from [E. O. Nadler et al. \(2025\)](#), the suppression of the subhalo mass function in WDM relative to CDM can also be expressed as

$$f_{\text{WDM}}(M, m_{\text{WDM}}) = \left[1 + \left(\frac{\alpha M_{\text{hm}}(m_{\text{WDM}})}{M} \right)^{\beta} \right]^{-\gamma}, \quad (12)$$

where $\alpha = 2.5$, $\beta = 0.9$ and $\gamma = 1.0$.

In Figure 1, we show the examples of the transfer functions and subhalo mass function suppressions for the FDM and WDM models with the same M_{hm} . We can see that, for fixed M_{hm} , the WDM exhibits a stronger suppression than the FDM at relatively high subhalo masses, whereas at lower masses its suppression becomes weaker than that of FDM.

3. OBSERVATIONAL DATA

We consider the observational data of satellite populations in both MW and M31 in the analysis. The observed MW satellite population used in this work is identical to that adopted in [E. O. Nadler et al. \(2020\)](#). It includes 18 satellites discovered in the PS1 DR1 data ([J. L. Tonry et al. 2012](#)) and 16 satellites identified in the DES Y3A2 data ([T. M. C. Abbott et al. 2018](#)), yielding a total of 34 MW satellites. The faintest satellite in this

sample, Cetus II, has absolute magnitude $M_V \simeq 0$ mag ([A. Drlica-Wagner et al. 2015](#)).

We use the DES and PS1 survey selection functions derived in [A. Drlica-Wagner et al. \(2020\)](#), which are publicly available as machine-learning classifiers. These classifiers predict the detection probability of a satellite as a function of its absolute magnitude M_V , heliocentric distance D , azimuthally averaged projected half-light radius $r_{1/2}$, and sky position. In addition, geometric constraints are applied to ensure that observable satellites lie within the survey footprints and to exclude regions where satellite detection is hindered by interstellar extinction, bright nearby stars, or bright extragalactic sources. We only consider satellites located within 300 kpc from the center of the MW. In addition, to exclude likely star clusters, we restrict our sample to satellites with $r_{1/2} > 10$ pc ([E. O. Nadler et al. 2020](#)).

The observed M31 satellite population used in this work is drawn from the PAndAS survey data ([A. Doliva-Dolinsky et al. 2023](#)). We adopt the analytic observational selection function developed by [A. Doliva-Dolinsky et al. \(2022\)](#). Although this selection function is analytic rather than a machine-learning classifier, it accounts for the dependence on absolute magnitude M_V , heliocentric distance D , azimuthally averaged projected half-light radius $r_{1/2}$, and sky position, with additional geometric constraints applied.

Thus, although the methods for deriving the MW and M31 selection functions differ, both frameworks are designed to accurately capture the detection probability as a function of the key satellite properties. We therefore do not expect this methodological difference to introduce significant systematic bias into the joint inference of our model parameters.

Specifically, our M31 satellite sample consists of the full set of 24 satellites used in [A. Doliva-Dolinsky et al. \(2023\)](#). The faintest satellite in our M31 sample is And XXVI, with an absolute magnitude of $M_V \simeq -6.0$ mag ([A. Savino et al. 2022](#)). Although And XXVI has a very low recovery fraction based on the selection function given in [A. Doliva-Dolinsky et al. \(2022\)](#), we have verified that including or excluding this system has a negligible impact on our results. Due to the PAndAS survey footprint, we only consider satellites located between 30 and 300 kpc from the center of M31. Because of the limitations of the selection function, we additionally restrict our analysis to satellites with $r_{1/2} > 63$ pc, although we have confirmed that our results are insensitive to this cut. In Figure 2, we show the half-light radii $r_{1/2}$ as a function of the absolute magnitudes M_V of all 58 satellite galaxies from DES, PS1, and PAndAS used in this work.

4. MODELING FRAMEWORK

In this section, we introduce our modeling framework based on the galaxy–halo connection model (E. O. Nadler et al. 2020), including the adopted dark matter-only zoom-in simulations, model parameters, and statistical inference procedure. More detailed description of the galaxy–halo connection model can be found in E. O. Nadler et al. (2019b) and E. O. Nadler et al. (2020).

4.1. Overview of the modeling framework

Our goal is to constrain dark matter models using the observed populations of satellite galaxies. To achieve this, we first construct a model capable of predicting satellite populations to fit the observational data. In this work, we use high-resolution dark matter-only zoom-in simulations based on CDM to generate subhalo populations. We then apply the galaxy–halo connection model to populate these subhalos with satellite galaxies. The impact of different dark matter models is introduced through the suppression of the subhalo mass function in non-CDM model relative to CDM. By varying the model parameters, we can thus generate predicted satellite populations.

After obtaining the predicted satellite populations, we convolve them with the observational selection functions, which quantify the probability of detecting satellites with different properties. This yields the predicted observable satellite populations. With these predictions, we employ a Poisson-based likelihood function combined with suitable priors to derive the posterior distributions of the model parameters.

It is important to note that our approach assumes that the radial distribution of satellites remains unchanged across different dark matter models. This assumption is justified for WDM (M. R. Lovell et al. 2014; S. Bose et al. 2017), while it is more uncertain for FDM. However, since the mean mass of the faintest satellites used in our analysis exceeds $10^8 M_\odot$ (E. O. Nadler et al. 2020), the wave interference effects of FDM can be safely neglected within the mass range of interest (S. May & V. Springel 2023; E. O. Nadler et al. 2025). Therefore, we consider this assumption is also reasonable for FDM.

4.2. Zoom-in simulations

We use high-resolution dark matter-only zoom-in simulations from Y.-Y. Mao et al. (2015), which are the same as those adopted in E. O. Nadler et al. (2020), to generate subhalo populations. The simulation suite contains 45 MW-mass host halos with virial masses between 1.18 and $1.57 \times 10^{12} M_\odot$. Subhalos in these simulations are well resolved down to a present-day maximum circular velocity of $V_{\text{max}} \approx 9 \text{ km s}^{-1}$. In addition, we require

each subhalo to have a peak maximum circular velocity $V_{\text{peak}} > 10 \text{ km s}^{-1}$.

Because the detailed merger history of the MW, particularly the early accretion of an galaxy with the Large Magellanic Cloud (LMC) mass, can affect its satellite population (S. Bose et al. 2020), we follow E. O. Nadler et al. (2020) and adopt two host halos with assembly histories similar to that of the MW, which have virial masses of 1.26 and $1.57 \times 10^{12} M_\odot$, respectively.

To avoid potential systematic uncertainties introduced by using different simulations, we use the same high-resolution dark matter-only zoom-in simulations from Y.-Y. Mao et al. (2015) for M31, even though its virial mass and merger history remain highly uncertain (M. Semećuk et al. 2018; R. P. van der Marel et al. 2019; E. Patel & K. S. Mandel 2023; X. Zhang et al. 2024; A. Doliva-Dolinsky et al. 2025). Specifically, we select two host halos with virial masses of 1.19 and $1.35 \times 10^{12} M_\odot$ to account for the uncertainty in M31 assembly history. We have verified that our results are insensitive to this choice, as using different simulated host halos yields similar constraints. We discuss our treatment of the large uncertainty in M31 virial mass in Section 4.3.

4.3. Model parameters and statistical inference

The galaxy–halo connection model includes eight parameters (E. O. Nadler et al. 2020). The first two parameters describe the mapping between the subhalo peak maximum circular velocity V_{peak} and the satellite absolute magnitude M_V : the power-law slope of the luminosity function, α , and the luminosity scatter, σ_M . The next two parameters characterize the galaxy formation efficiency using the subhalo peak virial mass M : the 50% galaxy occupation peak virial mass, \mathcal{M}_{50} , and the scatter in the galaxy occupation fraction, σ_{gal} . The fifth parameter, \mathcal{B} , quantifies the strength of subhalo disruption due to baryonic effects. The remaining three parameters describe the mapping between the subhalo virial radius at accretion and the satellite half-light radius $r_{1/2}$: the amplitude of the galaxy–halo size relation, \mathcal{A} , the scatter in half-light radius at fixed halo size, $\sigma_{\log_{10} R}$, and the power-law index of the size relation, n . We also introduce the parameter M_{hm} to model the effects of FDM or WDM (E. O. Nadler et al. 2021b). Its impact enters through the subhalo mass function suppression described by Equations (8) or (12), and M_{hm} can be converted into the corresponding dark matter particle mass using Equations (7) or (11).

Subhalo abundance is known to scale linearly with host halo mass (J. Wang et al. 2012; Y.-Y. Mao et al. 2015; C. Y. Tan et al. 2025b). In addressing the uncertainty in host halo mass, E. O. Nadler et al. (2020)

simply scale the final results based on the average mass of the two realistic MW-like simulations and the 2σ upper limit of the MW mass predicted in [T. M. Callingham et al. \(2019\)](#), yielding a very conservative result. In our work, we introduce the mass parameter M_{host} , which represents the virial mass of the MW or M31. This parameter linearly scales \mathcal{M}_{50} and M_{hm} relative to the simulated host halo mass M_{sim} , such that $\mathcal{M}_{50} = \mathcal{M}_{50}^{(\text{sim})}(M_{\text{host}}/M_{\text{sim}})$ and $M_{\text{hm}} = M_{\text{hm}}^{(\text{sim})}(M_{\text{host}}/M_{\text{sim}})$. We assign a log-normal prior within a 2σ range to the M_{host} parameter, so its role is to linearly scale \mathcal{M}_{50} and M_{hm} using the mass prior information, effectively accounting for the uncertainties in the MW and M31 masses.

For the MW, we use the results from [T. M. Callingham et al. \(2019\)](#), corresponding to $\log_{10}(M_{\text{MW}})$ in the range of [12.00, 12.26]. For M31, we adopt the baseline prior from [X. Zhang et al. \(2024\)](#), corresponding to $\log_{10}(M_{\text{M31}})$ in the range of [11.81, 12.45]. At the same time, we note that M31’s mass uncertainty is significant. The result from [E. Patel & K. S. Mandel \(2023\)](#) ($\sim 3.02 \times 10^{12} M_{\odot}$) is about a factor of 2-3 higher than our baseline setting from [X. Zhang et al. \(2024\)](#) ($\sim 1.33 \times 10^{12} M_{\odot}$). Therefore, we also consider the result from [E. Patel & K. S. Mandel \(2023\)](#), corresponding to $\log_{10}(M_{\text{M31}})$ in the range of [12.22, 12.74]. The priors for the other parameters are consistent with those in [E. O. Nadler et al. \(2025\)](#).

To account for uncertainty in the observer’s location, we fix the observer’s distance to 8 kpc for the MW ([E. O. Nadler et al. 2020](#)) and to 776 kpc for M31 ([A. Savino et al. 2022](#)), and then draw a random viewing position on the sphere at the corresponding radius. For MW realizations, we additionally rotate each simulated host halo, so that the LMC analog lies at the observed sky position of the LMC. For M31 realizations, we rotate the simulated system, so that the host center projects to the observed sky position of M31.

Therefore, for the MW or M31, given these 10 parameters θ and simulation data and using the binning method from [E. O. Nadler et al. \(2025\)](#), the number of predicted observable satellites in luminosity and surface brightness bin i in a given realization is

$$N_{\text{pred},i} = \sum_{s_i} p_{\text{detect},s_i} \times (1 - p_{\text{disrupt},s_i}) \times f_{\text{gal},s_i} \times f_{\text{non-CDM},s_i}, \quad (13)$$

where s_i represents the mock satellites in bin i , p_{detect,s_i} denotes the detection probability, which is determined by the observational selection functions, p_{disrupt,s_i} refers to the probability of disruption due to baryonic effects,

f_{gal,s_i} is the galaxy formation efficiency, and $f_{\text{non-CDM},s_i}$ represents the subhalo mass function suppression.

The probability of observing $N_{\text{obs},i}$ satellites in bin i is ([E. O. Nadler et al. 2019b, 2020](#))

$$P(N_{\text{obs},i}|\theta) = \left(\frac{N_{\text{real}} + 1}{N_{\text{real}}}\right)^{-(N_i+1)} \times (N_{\text{real}} + 1)^{-N_{\text{obs},i}} \frac{\Gamma(N_i + N_{\text{obs},i} + 1)}{\Gamma(N_{\text{obs},i} + 1)\Gamma(N_i + 1)}, \quad (14)$$

where N_{real} is the number of model realizations given θ and $N_i \equiv \sum_{j=1}^{N_{\text{real}}} N_{\text{pred},ij}$. For each simulated host halo, we generate 30 mock realizations corresponding to different absolute magnitudes, half-light radii, positions, and galaxy formation realizations. Because we use two simulated host halos for both the MW and M31 to account for uncertainties in their halo properties, this yields a total of $N_{\text{real}} = 60$ mock realizations. We have verified that 60 realizations are sufficient for convergence.

Before constructing the total likelihood function, we clarify that when jointly modeling the MW and M31 satellite populations, we treat \mathcal{M}_{50} , σ_{gal} , and M_{hm} as shared parameters, while all other parameters are allowed to vary independently for the MW and M31. We make this choice because the mass of M31 is highly uncertain and may exceed the mass range covered by our simulation suite ([Y.-Y. Mao et al. 2015](#); [E. Patel & K. S. Mandel 2023](#); [X. Zhang et al. 2024](#)). Although our galaxy–halo connection model is sufficiently flexible to reproduce the observed data even when the host mass lies outside the simulated range, the inferred parameters in such cases would be systematically biased (see Appendix A for a detailed discussion). In contrast, \mathcal{M}_{50} , σ_{gal} , and M_{hm} can be reliably scaled according to the mass priors, yielding physically consistent values.

We denote the MW- and M31-specific parameter sets by θ_{MW} and θ_{M31} and the shared parameters by θ_{share} . Given the vectors of observed satellite counts from DES, PS1, and PAndAS, $\mathbf{N}_{\text{DES}} = \{N_{\text{obs},i}^{\text{DES}}\}$, $\mathbf{N}_{\text{PS1}} = \{N_{\text{obs},i}^{\text{PS1}}\}$, and $\mathbf{N}_{\text{PA}} = \{N_{\text{obs},i}^{\text{PA}}\}$, the total likelihood is

$$P(\mathbf{N}_{\text{DES}}, \mathbf{N}_{\text{PS1}}, \mathbf{N}_{\text{PA}} | \theta_{\text{MW}}, \theta_{\text{M31}}, \theta_{\text{share}}) = \prod_{i \in \text{DES}} P(N_{\text{obs},i}^{\text{DES}} | \theta_{\text{MW}}, \theta_{\text{share}}) \prod_{i \in \text{PS1}} P(N_{\text{obs},i}^{\text{PS1}} | \theta_{\text{MW}}, \theta_{\text{share}}) \times \prod_{i \in \text{PA}} P(N_{\text{obs},i}^{\text{PA}} | \theta_{\text{M31}}, \theta_{\text{share}}), \quad (15)$$

where $P(\cdot|\cdot)$ is the per-bin likelihood in Equation (14) with the expected counts given by Equation (13). The joint posterior over all parameters is

$$P(\theta_{\text{MW}}, \theta_{\text{M31}}, \theta_{\text{share}} | \mathbf{N}_{\text{DES}}, \mathbf{N}_{\text{PS1}}, \mathbf{N}_{\text{PA}}) \propto P(\mathbf{N}_{\text{DES}}, \mathbf{N}_{\text{PS1}}, \mathbf{N}_{\text{PA}} | \theta_{\text{MW}}, \theta_{\text{M31}}, \theta_{\text{share}}) \times \pi_{\text{MW}}(\theta_{\text{MW}}) \pi_{\text{M31}}(\theta_{\text{M31}}) \pi_{\text{share}}(\theta_{\text{share}}), \quad (16)$$

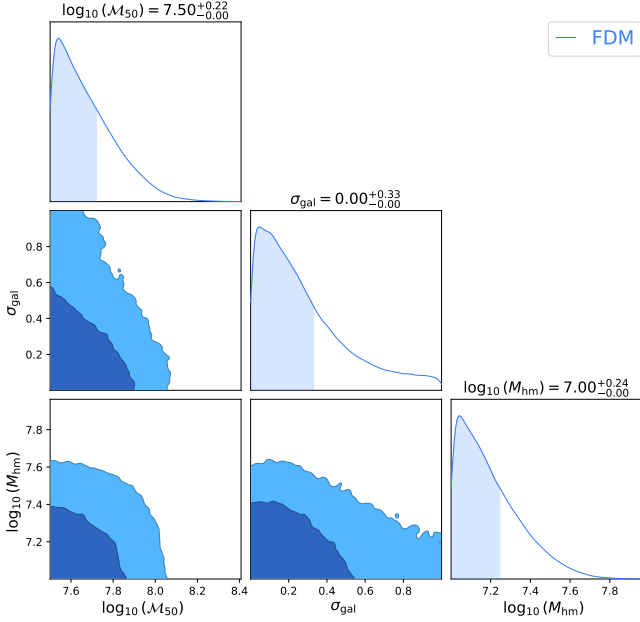


Figure 3. The PDF and contour maps (68% and 95% CLs) of the shared parameters in the FDM model. The shaded regions in the one-dimensional PDFs and the quoted parameter values correspond to 68% CL. The parameters M_{50} and M_{hm} are in units of M_{\odot} , and σ_{gal} is in dex.

where $\pi_{\text{MW}}(\theta_{\text{MW}})$ and $\pi_{\text{M31}}(\theta_{\text{M31}})$ are the priors for the MW- and M31-specific parameters, and $\pi_{\text{share}}(\theta_{\text{share}})$ is the prior for the shared parameters. The normalization constant (evidence) is omitted as it is independent of the parameters. The marginal posterior for the shared parameters is:

$$P(\theta_{\text{share}} | \mathbf{N}_{\text{DES}}, \mathbf{N}_{\text{PS1}}, \mathbf{N}_{\text{PA}}) = \int d\theta_{\text{MW}} \int d\theta_{\text{M31}} P(\theta_{\text{MW}}, \theta_{\text{M31}}, \theta_{\text{share}} | \mathbf{N}_{\text{DES}}, \mathbf{N}_{\text{PS1}}, \mathbf{N}_{\text{PA}}). \quad (17)$$

We use **emcee** (D. Foreman-Mackey et al. 2013) in the constraint process for the model parameters. Specifically, we run 112 walkers for 10^5 steps, and retain more than 10^4 independent samples overall to sample the posterior or probability distribution functions (PDFs) of the parameters.

5. CONSTRAINT RESULTS

5.1. Fuzzy dark matter

In Figure 3, we show the marginalized PDFs and contour maps for the shared parameters in the FDM model. From the PDFs, we derive $M_{\text{hm}} < 3.10 \times 10^7 M_{\odot}$ at 95% confidence level (CL), which can be converted into a lower limit on the FDM particle mass using Equation (7), yielding

$$m_{\text{FDM}} > 1.75 \times 10^{-20} \text{ eV (95\% CL)}. \quad (18)$$

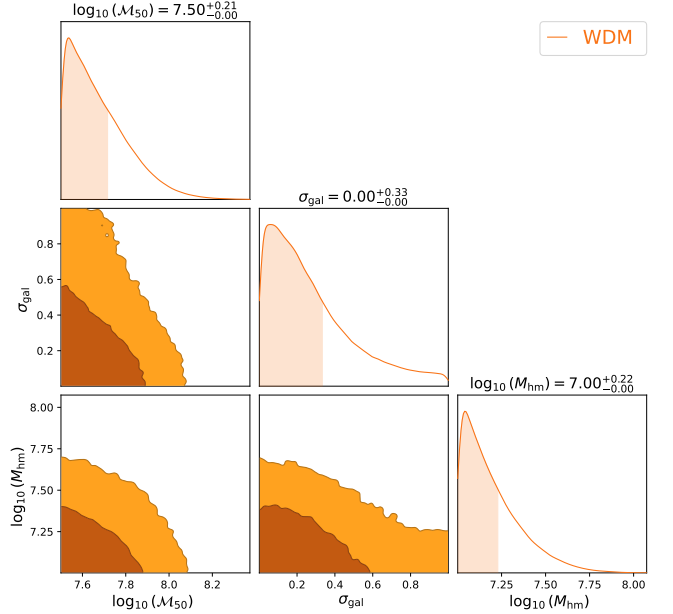


Figure 4. Same as Figure 3, but for the WDM case.

This constraint improves upon the result obtained using only the MW satellite population by E. O. Nadler et al. (2025), $m_{\text{FDM}} > 1.4 \times 10^{-20}$ eV, by about 25%. The precision of our limit is also comparable to that from the Lyman- α forest analysis in K. K. Rogers & H. V. Peiris (2021), which yields $m_{\text{FDM}} > 2.0 \times 10^{-20}$ eV.

Besides, to obtain a more prior-independent constraint, we also adopt a posterior ratio of 20:1, corresponding to the point where the posterior probability drops to one-twentieth of its maximum value (D. M. Powell et al. 2023; R. E. Keeley et al. 2024; C. Y. Tan et al. 2025a). Our lower prior bound on M_{hm} , $10^7 M_{\odot}$, coincides with the region where the posterior distribution flattens out, and we have verified the robustness of the 20:1 posterior ratio result by varying the prior range. For the FDM case, this criterion yields $M_{\text{hm}} < 4.19 \times 10^7 M_{\odot}$, corresponding to

$$m_{\text{FDM}} > 1.41 \times 10^{-20} \text{ eV (20:1 posterior ratio)}. \quad (19)$$

Our result is about three times stronger than the posterior odds ratio of 20:1 constraint derived from strong gravitational lensing by D. M. Powell et al. (2023), who obtained $m_{\text{FDM}} > 4.4 \times 10^{-21}$ eV. We note that D. M. Powell et al. (2023) and C. Y. Tan et al. (2025a) adopt a posterior odds ratio, while E. O. Nadler et al. (2021a) use a likelihood ratio. However, because our posterior flattens toward the lower prior boundary and we adopt a uniform prior in $\log_{10}(M_{\text{hm}})$, these criteria reduce to the same effective threshold as our posterior ratio.

We present the full PDFs and contour maps of the MW and M31 parameters for the FDM case in Appendix A. We have verified that, aside from the shared

parameters, the posterior distributions of the other parameters are consistent with those obtained from the separate MW and M31 fits. Furthermore, we rerun our model using the larger M31 mass prior from [E. Patel & K. S. Mandel \(2023\)](#), and obtain similar and slightly weaker constraint results with $m_{\text{FDM}} > 1.69 \times 10^{-20}$ eV (95% CL) and $m_{\text{FDM}} > 1.37 \times 10^{-20}$ eV (20:1 posterior ratio).

5.2. Warm dark matter

Figure 4 shows the marginalized PDFs and contour maps of the shared parameters in the WDM model. The marginalized posterior yields $M_{\text{hm}} < 3.20 \times 10^7 M_{\odot}$ at 95% CL, corresponding to a lower limit on the WDM particle mass using Equation (11), and we have

$$m_{\text{WDM}} > 6.22 \text{ keV (95\% CL)}. \quad (20)$$

This constraint represents a $\sim 5\%$ improvement over the result obtained using only the MW satellite population by [E. O. Nadler et al. \(2025\)](#) with $m_{\text{WDM}} > 5.9$ keV. At a posterior ratio of 20:1, we obtain $M_{\text{hm}} < 4.24 \times 10^7 M_{\odot}$, corresponding to

$$m_{\text{WDM}} > 5.75 \text{ keV (20:1 posterior ratio)}. \quad (21)$$

Since the posterior distributions for all parameters in the WDM case are very similar to those in the FDM case, we do not provide figures showing the posterior distributions of all the MW and M31 parameters for the WDM case. We also rerun our model using the larger M31 mass prior from [E. Patel & K. S. Mandel \(2023\)](#), obtaining $m_{\text{WDM}} > 6.10$ keV (95% CL) and $m_{\text{WDM}} > 5.63$ keV (20:1 posterior ratio).

We note that in [E. O. Nadler et al. \(2025\)](#), the inferred M_{hm} for WDM is slightly lower than that for FDM, whereas our results show the opposite trend. This difference also explains why our improvement in the WDM constraint is only marginal. A possible reason is that our number of realizations, N_{real} , is much larger than that used in [E. O. Nadler et al. \(2025\)](#), making our model more sensitive to subtle differences in the subhalo population. As shown in Figure 1, at the most sensitive mass scale around $10^8 M_{\odot}$, the subhalo mass function for WDM is slightly higher than that for FDM at the same M_{hm} . To compensate for this difference, the inferred M_{hm} for WDM tends to be slightly larger, resulting in the extended tail as shown in Figure 4.

Compared to [E. O. Nadler et al. \(2025\)](#), our improvements arise mainly from two aspects: first, we adopt a more flexible mass-scaling approach; second, we include the M31 satellite population in our joint analysis. Since the constraints are primarily sensitive to the

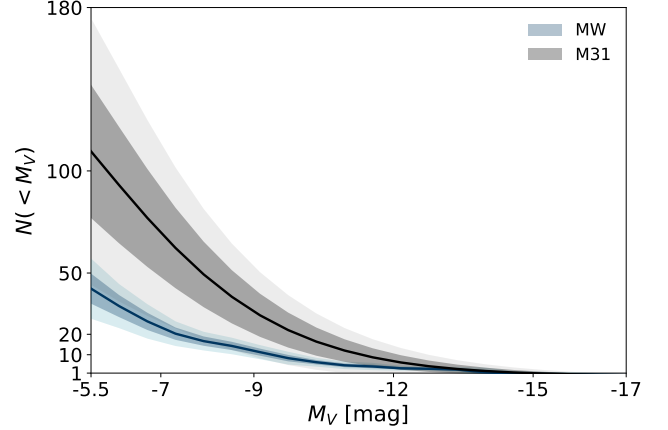


Figure 5. Luminosity functions of satellites located between 30 and 300 kpc from the centers of the MW (blue) and M31 (gray), based on the FDM results from our modeling framework. Dark and light shaded regions show the 68% and 95% CLs, and the black solid lines denotes the mean predicted luminosity functions.

faintest satellites, incorporating the M31 satellite population strengthens the limits only at the few-percent level, which we summarize as an overall improvement of $\sim 10\%$ relative to using the MW sample alone. Moreover, because the mass and accretion history of M31 are highly uncertain, we do not treat all parameters as shared parameters, as was done in [E. O. Nadler et al. \(2024\)](#), when presenting our final constraints. We have verified that treating all parameters as shared would further tighten the constraints by about 5% relative to our adopted approach.

6. ADDITIONAL RESULTS AND DISCUSSION

6.1. Luminosity functions of the MW and M31

Using the posterior distributions inferred from our modeling framework, and adopting the FDM results as a representative case, we predict the satellite luminosity functions for both the MW and M31 (see Figure 5). Within the range $-20 < M_V < -5.5$ and distances of $30 \text{ kpc} < R < 300 \text{ kpc}$ from the centers of the MW or M31, we obtain 42 ± 7 satellites for the MW and 110 ± 33 for M31. These results are consistent with the estimates from [C. Y. Tan et al. \(2025b\)](#), who found 29^{+9}_{-7} MW satellites, and from [A. Doliva-Dolinsky et al. \(2023\)](#), who obtained 136^{+65}_{-35} or 92^{+19}_{-26} M31 satellites, depending on the assumed spatial distribution.

We find that the number of M31 satellites is approximately three times that of the MW, which is consistent with the findings given by [C. Y. Tan et al. \(2025b\)](#). Considering that satellite abundance is known to scale roughly linearly with host halo mass, this may suggest that M31 is about three times more massive than the

MW, in agreement with the estimate from E. Patel & K. S. Mandel (2023). However, the enhanced satellite abundance around M31 may also be partly explained by its past interaction with M33 (S. C. Chapman et al. 2013; A. Doliva-Dolinsky et al. 2025).

6.2. Anisotropy in the M31 satellite distribution

As more M31 satellites have been discovered, it has become evident that their spatial distribution may be not isotropic. Specifically, among the 24 M31 satellites used in this work, only three are located on the side opposite the MW (A. Savino et al. 2022; A. Doliva-Dolinsky et al. 2023). To examine whether this anisotropy could arise from observational selection effects, we use the posterior distributions inferred from our modeling framework to simulate 10^5 realizations, each representing an observation of 24 M31 satellites.

We then obtain the PDF and cumulative distribution function (CDF) of the number of satellites located opposite the MW (see Figure 6). In all 10^5 simulated realizations, none produce as few as three satellites on the far side. Even the probability of having eight satellites on the far side corresponds to a CDF value below 0.05. This indicates that, even after accounting for distance uncertainties, the observed distribution cannot be explained by selection effects alone, consistent with the conclusions of previous studies (A. Savino et al. 2022; A. Doliva-Dolinsky et al. 2023; K. J. Kanehisa et al. 2025). Interestingly, although detectability decreases with increasing distance, the larger observable volume counteracts this decline. As a result, if the M31 satellite distribution is isotropic, the probability of detecting more satellites on the far side than on the near side would in fact be slightly greater than 50%. Finally, we note that the strong anisotropy of the M31 satellites may, in principle, affect abundance-based constraints, but no reliable framework currently exists to incorporate this effect. In our analysis, we do not include any spatial information in our binning scheme. We have also verified that using different simulated host halos yields consistent constraints within our modeling framework. We will explore this issue in more detail in future work.

7. SUMMARY AND OUTLOOK

In this work, we develop a modeling framework and perform a joint analysis of the MW and M31 satellite systems to study the properties of both FDM and WDM. We use the galaxy–halo connection model together with the updated transfer functions and subhalo mass functions to construct the framework, and adopt the observational data of MW and M31 satellite galaxies from DES, PS1, and PAndAS, including their corresponding

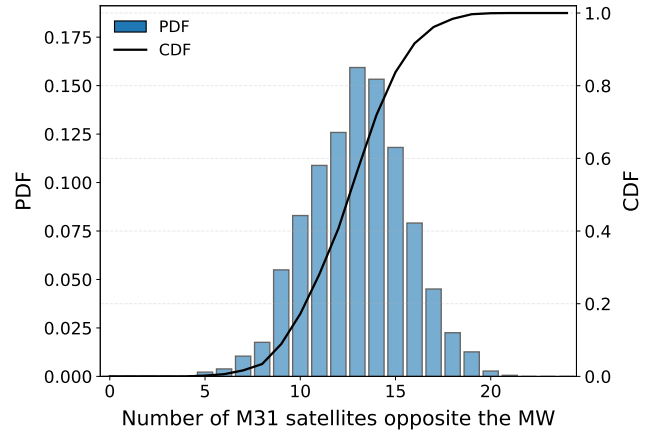


Figure 6. The PDF (blue histogram) and CDF (black curve) of the number of M31 satellites located on the side opposite the MW, based on 10^5 simulated realizations conditioned on the 24 observed satellites, using the FDM results from our modeling framework.

selection functions. We further account for the uncertain virial masses of the MW and M31 by introducing priors on their host halo masses and linearly scaling the relevant model parameters.

We find that, for the FDM case, $m_{\text{FDM}} > 1.75 \times 10^{-20}$ eV (95% CL) and $m_{\text{FDM}} > 1.41 \times 10^{-20}$ eV (20:1 posterior ratio). For thermal-relic WDM, we find $m_{\text{WDM}} > 6.22$ keV (95% CL) and $m_{\text{WDM}} > 5.75$ keV (20:1 posterior ratio). These results represent a moderate improvement over the MW-only constraints given by the previous works. Our analysis therefore provides the strongest constraints to date on FDM and WDM models derived from satellite galaxy populations in the Local Group. We also verify that adopting extreme assumptions for the mass of M31 weakens our constraints only slightly. These limits can be combined with complementary probes such as strong gravitational lensing and the Lyman- α forest to achieve even tighter bounds (E. O. Nadler et al. 2021a; W. Enzi et al. 2021).

Looking ahead, next-generation surveys such as the Rubin Observatory Legacy Survey of Space and Time (LSST; K. Tsiane et al. 2025), Chinese Space Station Survey Telescope (CSST; H. Qu et al. 2023; CSST Collaboration et al. 2025), and Dark Energy Spectroscopic Instrument (DESI; A. Dey et al. 2023) will greatly expand the known satellite populations in the Local Group, including systems fainter than those currently detected. In addition, these surveys will also improve measurements of the virial masses and accretion histories of the MW and M31. Combined with advances in high-precision, large-volume dark-matter simulations that probe a broader range of host masses and assembly histories, as well as continued progress in observa-

tional selection functions, future analyses will be able to achieve more accurate constraints on the properties of dark matter.

ACKNOWLEDGMENTS

We thank Ethan Nadler for the help with implementing the galaxy–halo connection model code. J.X.L. and Y.G. acknowledge the support from National Key R&D Program of China grant Nos. 2022YFF0503404 and 2020SKA0110402, and the CAS Project for Young Scientists in Basic Research (No. YSBR-092). KL was

supported by National Key R&D Programme of China (no. 2024YFC2207400). This work is also supported by science research grants from the China Manned Space Project with grant Nos. CMS-CSST-2025-A02, CMS-CSST-2021-B01, and CMS-CSST-2021-A01.

Software: `Astropy` (Astropy Collaboration et al. 2013, 2018, 2022), `ChainConsumer` (S. R. Hinton 2016), `emcee` (D. Foreman-Mackey et al. 2013), `healpy` (K. M. Górski et al. 2005; A. Zonca et al. 2019), `Matplotlib` (J. D. Hunter 2007), `NumPy` (C. R. Harris et al. 2020), `pandas` (Wes McKinney 2010; T. pandas development team 2020), `SciPy` (P. Virtanen et al. 2020)

APPENDIX

A. POSTERIOR DISTRIBUTIONS OF MODEL PARAMETERS

In Figures 7 and 8, we show the PDFs and contour maps (68% and 95% CLs) of the MW and M31 parameters for the FDM case, using the model introduced in Section 4. We do not show the M_{host} parameter because its posterior closely follows the adopted prior.

As discussed in Section 4.3, the posterior distributions of the M31-specific parameters inferred from our model are likely to be biased. This is because the virial mass of M31 is probably larger than the mass range of the simulated host halos we use, and its accretion history remains highly uncertain (M. Semczuk et al. 2018; R. P. van der Marel et al. 2019; E. Patel & K. S. Mandel 2023; X. Zhang et al. 2024; A. Doliva-Dolinsky et al. 2025). As shown in Figures 7 and 8, the MW and M31 exhibit significant differences in three parameters: the power-law slope of the luminosity function, α , the luminosity scatter, σ_M , and the amplitude of the galaxy–halo size relation, \mathcal{A} . This behavior is consistent with our expectations.

However, the faintest satellite in our M31 sample has an absolute magnitude of $M_V \simeq -6.0$ mag, while the faintest MW satellite reaches $M_V \simeq 0$ mag. The absolute magnitude of $M_V \simeq -6.0$ mag lies at the luminosity scale that is most sensitive to the reionization. Therefore, the fainter systems, which in our model appear only among the MW satellites, tend to form most of their stars before reionization. As a result, they develop more compact stellar distributions and deviate from the general size–luminosity relation (V. Manwadkar & A. V. Kravtsov 2022; C. Y. Tan et al. 2025b; A. Doliva-Dolinsky et al. 2025). Their luminosity function may also deviate from a simple power law (S. Bose et al. 2018; V. Manwadkar & A. V. Kravtsov 2022). This effect could partially explain the differences in the inferred parameters between the MW and M31. To test this, we rerun our model using only MW satellites with $M_V < -6.0$. Although the parameter uncertainties increase due to the reduced data size, the discrepancy between the MW and M31 parameters decreases to some extent (with noticeable shifts in their maximum-posterior values), especially for the amplitude of the galaxy–halo size relation, \mathcal{A} .

REFERENCES

- Abbott, T. M. C., Abdalla, F. B., Allam, S., et al. 2018, *ApJS*, 239, 18, doi: [10.3847/1538-4365/aae9f0](https://doi.org/10.3847/1538-4365/aae9f0)
- Astropy Collaboration, Robitaille, T. P., Tollerud, E. J., et al. 2013, *A&A*, 558, A33, doi: [10.1051/0004-6361/201322068](https://doi.org/10.1051/0004-6361/201322068)
- Astropy Collaboration, Price-Whelan, A. M., Sipőcz, B. M., et al. 2018, *AJ*, 156, 123, doi: [10.3847/1538-3881/aabc4f](https://doi.org/10.3847/1538-3881/aabc4f)
- Astropy Collaboration, Price-Whelan, A. M., Lim, P. L., et al. 2022, *ApJ*, 935, 167, doi: [10.3847/1538-4357/ac7c74](https://doi.org/10.3847/1538-4357/ac7c74)
- Bode, P., Ostriker, J. P., & Turok, N. 2001, *ApJ*, 556, 93, doi: [10.1086/321541](https://doi.org/10.1086/321541)
- Boehm, C., Fayet, P., & Schaeffer, R. 2001, *Physics Letters B*, 518, 8, doi: [10.1016/S0370-2693\(01\)01060-7](https://doi.org/10.1016/S0370-2693(01)01060-7)
- Bose, S., Deason, A. J., Belokurov, V., & Frenk, C. S. 2020, *MNRAS*, 495, 743, doi: [10.1093/mnras/staa1199](https://doi.org/10.1093/mnras/staa1199)
- Bose, S., Deason, A. J., & Frenk, C. S. 2018, *ApJ*, 863, 123, doi: [10.3847/1538-4357/aabc44](https://doi.org/10.3847/1538-4357/aabc44)

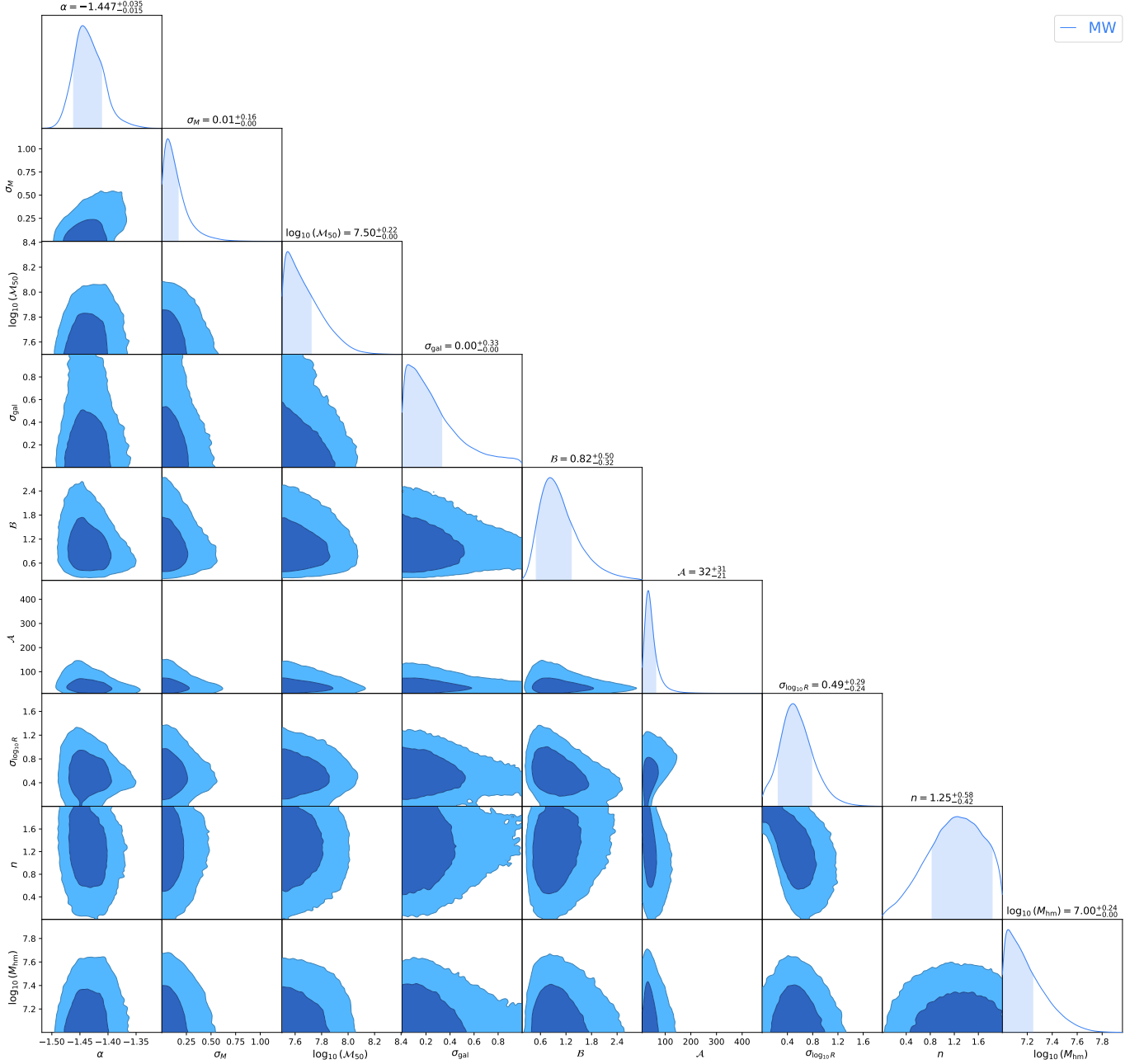


Figure 7. The PDF and contour maps (68% and 95% CLs) of the MW parameters for the FDM case. The shaded regions in the one-dimensional marginalized PDFs and the parameter summaries denote 68% CL. The parameters σ_M , σ_{gal} , and $\sigma_{\log_{10} R}$ are in dex, M_{50} and M_{hm} are in units of M_{\odot} , A is reported in pc, and α , n , and β are dimensionless.

Bose, S., Hellwing, W. A., Frenk, C. S., et al. 2017,

MNRAS, 464, 4520, doi: [10.1093/mnras/stw2686](https://doi.org/10.1093/mnras/stw2686)

Boyaarsky, A., Drewes, M., Lasserre, T., Mertens, S., & Ruchayskiy, O. 2019, Progress in Particle and Nuclear Physics, 104, 1, doi: [10.1016/j.ppnp.2018.07.004](https://doi.org/10.1016/j.ppnp.2018.07.004)

Bryan, G. L., & Norman, M. L. 1998, ApJ, 495, 80, doi: [10.1086/305262](https://doi.org/10.1086/305262)

Callingham, T. M., Cautun, M., Deason, A. J., et al. 2019, MNRAS, 484, 5453, doi: [10.1093/mnras/stz365](https://doi.org/10.1093/mnras/stz365)

Chambers, K. C., Magnier, E. A., Metcalfe, N., et al. 2016, arXiv e-prints, arXiv:1612.05560,

doi: [10.48550/arXiv.1612.05560](https://doi.org/10.48550/arXiv.1612.05560)

Chapman, S. C., Widrow, L., Collins, M. L. M., et al. 2013, MNRAS, 430, 37, doi: [10.1093/mnras/sts392](https://doi.org/10.1093/mnras/sts392)

CSST Collaboration, Gong, Y., Miao, H., et al. 2025, arXiv e-prints, arXiv:2507.04618,

doi: [10.48550/arXiv.2507.04618](https://doi.org/10.48550/arXiv.2507.04618)

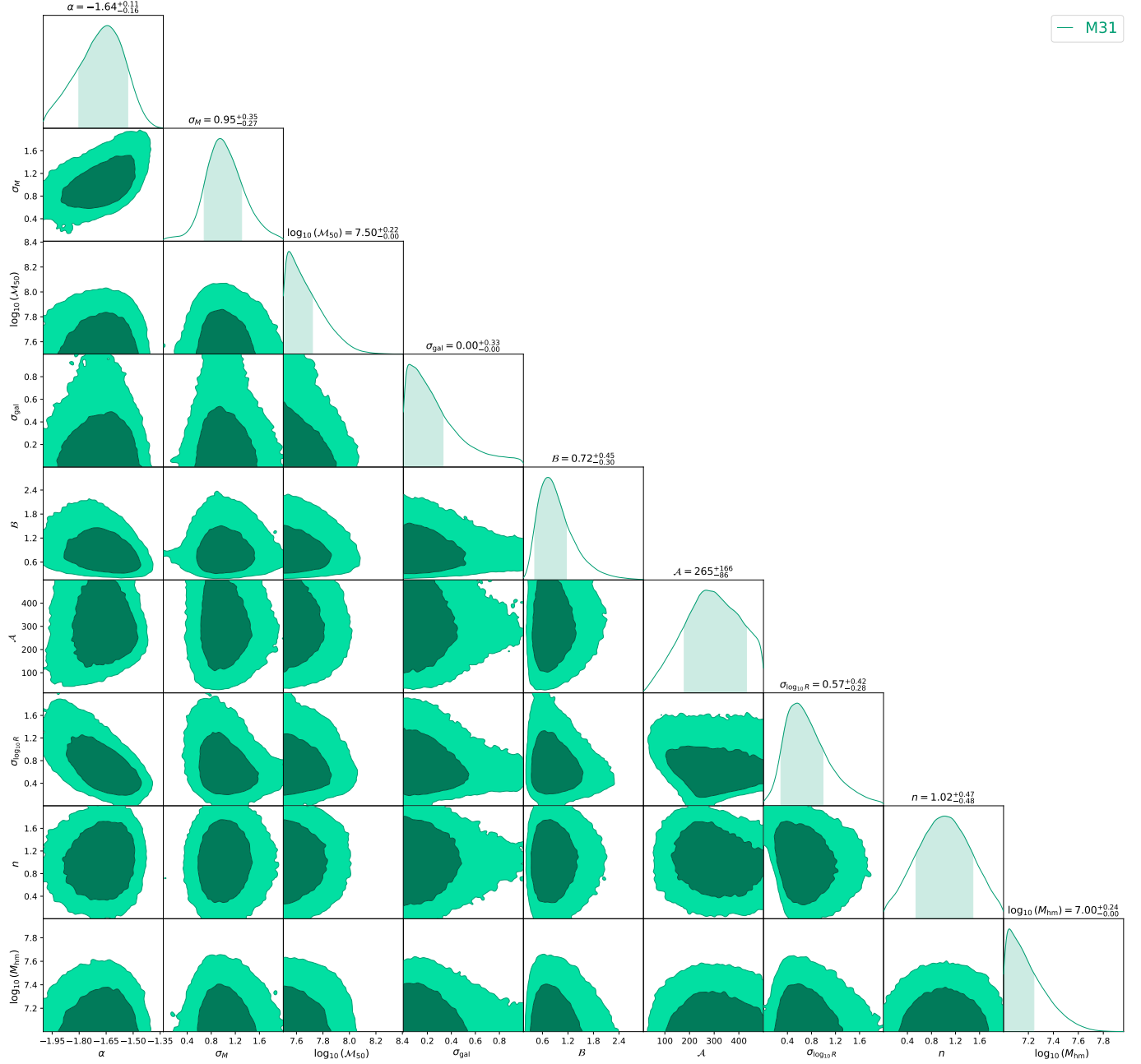


Figure 8. Same as Figure 7, but for the M31 case.

Dark Energy Survey Collaboration, Abbott, T., Abdalla, F. B., et al. 2016, MNRAS, 460, 1270, doi: [10.1093/mnras/stw641](https://doi.org/10.1093/mnras/stw641)

Dekker, A., Ando, S., Correa, C. A., & Ng, K. C. Y. 2022, PhRvD, 106, 123026, doi: [10.1103/PhysRevD.106.123026](https://doi.org/10.1103/PhysRevD.106.123026)

Del Popolo, A., & Le Delliou, M. 2017, Galaxies, 5, 17, doi: [10.3390/galaxies5010017](https://doi.org/10.3390/galaxies5010017)

Dey, A., Najita, J. R., Kposov, S. E., et al. 2023, ApJ, 944, 1, doi: [10.3847/1538-4357/aca5f8](https://doi.org/10.3847/1538-4357/aca5f8)

Doliva-Dolinsky, A., Collins, M. L. M., & Martin, N. F. 2025, arXiv e-prints, arXiv:2502.06948, doi: [10.48550/arXiv.2502.06948](https://doi.org/10.48550/arXiv.2502.06948)

Doliva-Dolinsky, A., Martin, N. F., Thomas, G. F., et al. 2022, ApJ, 933, 135, doi: [10.3847/1538-4357/ac6fd5](https://doi.org/10.3847/1538-4357/ac6fd5)

Doliva-Dolinsky, A., Martin, N. F., Yuan, Z., et al. 2023, ApJ, 952, 72, doi: [10.3847/1538-4357/acdcf6](https://doi.org/10.3847/1538-4357/acdcf6)

Drlica-Wagner, A., Bechtol, K., Rykoff, E. S., et al. 2015, ApJ, 813, 109, doi: [10.1088/0004-637X/813/2/109](https://doi.org/10.1088/0004-637X/813/2/109)

Drlica-Wagner, A., Bechtol, K., Mau, S., et al. 2020, ApJ, 893, 47, doi: [10.3847/1538-4357/ab7eb9](https://doi.org/10.3847/1538-4357/ab7eb9)

- Eberhardt, A., & Ferreira, E. G. M. 2025, arXiv e-prints, arXiv:2507.00705, doi: [10.48550/arXiv.2507.00705](https://doi.org/10.48550/arXiv.2507.00705)
- Enzi, W., Murgia, R., Newton, O., et al. 2021, MNRAS, 506, 5848, doi: [10.1093/mnras/stab1960](https://doi.org/10.1093/mnras/stab1960)
- Foreman-Mackey, D., Hogg, D. W., Lang, D., & Goodman, J. 2013, PASP, 125, 306, doi: [10.1086/670067](https://doi.org/10.1086/670067)
- Gluscevic, V., & Boddy, K. K. 2018, PhRvL, 121, 081301, doi: [10.1103/PhysRevLett.121.081301](https://doi.org/10.1103/PhysRevLett.121.081301)
- Górski, K. M., Hivon, E., Banday, A. J., et al. 2005, ApJ, 622, 759, doi: [10.1086/427976](https://doi.org/10.1086/427976)
- Harris, C. R., Millman, K. J., van der Walt, S. J., et al. 2020, Nature, 585, 357, doi: [10.1038/s41586-020-2649-2](https://doi.org/10.1038/s41586-020-2649-2)
- Hinshaw, G., Larson, D., Komatsu, E., et al. 2013, ApJS, 208, 19, doi: [10.1088/0067-0049/208/2/19](https://doi.org/10.1088/0067-0049/208/2/19)
- Hinton, S. R. 2016, The Journal of Open Source Software, 1, 00045, doi: [10.21105/joss.00045](https://doi.org/10.21105/joss.00045)
- Hu, W., Barkana, R., & Gruzinov, A. 2000, PhRvL, 85, 1158, doi: [10.1103/PhysRevLett.85.1158](https://doi.org/10.1103/PhysRevLett.85.1158)
- Hui, L. 2021, ARA&A, 59, 247, doi: [10.1146/annurev-astro-120920-010024](https://doi.org/10.1146/annurev-astro-120920-010024)
- Hunter, J. D. 2007, Computing in Science & Engineering, 9, 90, doi: [10.1109/MCSE.2007.55](https://doi.org/10.1109/MCSE.2007.55)
- Jungman, G., Kamionkowski, M., & Griest, K. 1996, PhR, 267, 195, doi: [10.1016/0370-1573\(95\)00058-5](https://doi.org/10.1016/0370-1573(95)00058-5)
- Kanehisa, K. J., Pawlowski, M. S., & Libeskind, N. 2025, Nature Astronomy, 9, 692, doi: [10.1038/s41550-025-02480-3](https://doi.org/10.1038/s41550-025-02480-3)
- Keeley, R. E., Nierenberg, A. M., Gilman, D., et al. 2024, MNRAS, 535, 1652, doi: [10.1093/mnras/stae2458](https://doi.org/10.1093/mnras/stae2458)
- Lovell, M. R., Frenk, C. S., Eke, V. R., et al. 2014, MNRAS, 439, 300, doi: [10.1093/mnras/stt2431](https://doi.org/10.1093/mnras/stt2431)
- Manwadkar, V., & Kravtsov, A. V. 2022, MNRAS, 516, 3944, doi: [10.1093/mnras/stac2452](https://doi.org/10.1093/mnras/stac2452)
- Mao, Y.-Y., Williamson, M., & Wechsler, R. H. 2015, ApJ, 810, 21, doi: [10.1088/0004-637X/810/1/21](https://doi.org/10.1088/0004-637X/810/1/21)
- Marsh, D. J. E., & Niemeyer, J. C. 2019, PhRvL, 123, 051103, doi: [10.1103/PhysRevLett.123.051103](https://doi.org/10.1103/PhysRevLett.123.051103)
- May, S., & Springel, V. 2023, MNRAS, 524, 4256, doi: [10.1093/mnras/stad2031](https://doi.org/10.1093/mnras/stad2031)
- McConnachie, A. W., Irwin, M. J., Ibata, R. A., et al. 2009, Nature, 461, 66, doi: [10.1038/nature08327](https://doi.org/10.1038/nature08327)
- McConnachie, A. W., Ibata, R., Martin, N., et al. 2018, ApJ, 868, 55, doi: [10.3847/1538-4357/aae8e7](https://doi.org/10.3847/1538-4357/aae8e7)
- Nadler, E. O., An, R., Gluscevic, V., Benson, A., & Du, X. 2025, ApJ, 986, 127, doi: [10.3847/1538-4357/adceef](https://doi.org/10.3847/1538-4357/adceef)
- Nadler, E. O., Birrer, S., Gilman, D., et al. 2021a, ApJ, 917, 7, doi: [10.3847/1538-4357/abf9a3](https://doi.org/10.3847/1538-4357/abf9a3)
- Nadler, E. O., Gluscevic, V., Boddy, K. K., & Wechsler, R. H. 2019a, ApJL, 878, L32, doi: [10.3847/2041-8213/ab1eb2](https://doi.org/10.3847/2041-8213/ab1eb2)
- Nadler, E. O., Gluscevic, V., Driskell, T., et al. 2024, ApJ, 967, 61, doi: [10.3847/1538-4357/ad3bb1](https://doi.org/10.3847/1538-4357/ad3bb1)
- Nadler, E. O., Mao, Y.-Y., Green, G. M., & Wechsler, R. H. 2019b, ApJ, 873, 34, doi: [10.3847/1538-4357/ab040e](https://doi.org/10.3847/1538-4357/ab040e)
- Nadler, E. O., Wechsler, R. H., Bechtol, K., et al. 2020, ApJ, 893, 48, doi: [10.3847/1538-4357/ab846a](https://doi.org/10.3847/1538-4357/ab846a)
- Nadler, E. O., Drlica-Wagner, A., Bechtol, K., et al. 2021b, PhRvL, 126, 091101, doi: [10.1103/PhysRevLett.126.091101](https://doi.org/10.1103/PhysRevLett.126.091101)
- Nelson, D., Pillepich, A., Springel, V., et al. 2018, MNRAS, 475, 624, doi: [10.1093/mnras/stx3040](https://doi.org/10.1093/mnras/stx3040)
- Newton, O., Cautun, M., Jenkins, A., Frenk, C. S., & Helly, J. C. 2018, MNRAS, 479, 2853, doi: [10.1093/mnras/sty1085](https://doi.org/10.1093/mnras/sty1085)
- Newton, O., Leo, M., Cautun, M., et al. 2021, JCAP, 2021, 062, doi: [10.1088/1475-7516/2021/08/062](https://doi.org/10.1088/1475-7516/2021/08/062)
- pandas development team, T. 2020, pandas-dev/pandas: Pandas, latest Zenodo, doi: [10.5281/zenodo.3509134](https://doi.org/10.5281/zenodo.3509134)
- Passaglia, S., & Hu, W. 2022, PhRvD, 105, 123529, doi: [10.1103/PhysRevD.105.123529](https://doi.org/10.1103/PhysRevD.105.123529)
- Patel, E., & Mandel, K. S. 2023, ApJ, 948, 104, doi: [10.3847/1538-4357/acc029](https://doi.org/10.3847/1538-4357/acc029)
- Planck Collaboration, Aghanim, N., Akrami, Y., et al. 2020a, A&A, 641, A6, doi: [10.1051/0004-6361/201833910](https://doi.org/10.1051/0004-6361/201833910)
- Planck Collaboration, Aghanim, N., Akrami, Y., et al. 2020b, A&A, 641, A1, doi: [10.1051/0004-6361/201833880](https://doi.org/10.1051/0004-6361/201833880)
- Powell, D. M., Vegetti, S., McKean, J. P., et al. 2023, MNRAS, 524, L84, doi: [10.1093/mnras/lsad074](https://doi.org/10.1093/mnras/lsad074)
- Qu, H., Yuan, Z., Doliva-Dolinsky, A., et al. 2023, MNRAS, 523, 876, doi: [10.1093/mnras/stad1352](https://doi.org/10.1093/mnras/stad1352)
- Rogers, K. K., & Peiris, H. V. 2021, PhRvL, 126, 071302, doi: [10.1103/PhysRevLett.126.071302](https://doi.org/10.1103/PhysRevLett.126.071302)
- Savino, A., Weisz, D. R., Skillman, E. D., et al. 2022, ApJ, 938, 101, doi: [10.3847/1538-4357/ac91cb](https://doi.org/10.3847/1538-4357/ac91cb)
- Schneider, A., Smith, R. E., Macciò, A. V., & Moore, B. 2012, MNRAS, 424, 684, doi: [10.1111/j.1365-2966.2012.21252.x](https://doi.org/10.1111/j.1365-2966.2012.21252.x)
- Semczuk, M., Lokas, E. L., Salomon, J.-B., Athanassoula, E., & D’Onghia, E. 2018, ApJ, 864, 34, doi: [10.3847/1538-4357/aad4ae](https://doi.org/10.3847/1538-4357/aad4ae)
- Tan, C. Y., Dekker, A., & Drlica-Wagner, A. 2025a, PhRvD, 111, 063079, doi: [10.1103/PhysRevD.111.063079](https://doi.org/10.1103/PhysRevD.111.063079)
- Tan, C. Y., Drlica-Wagner, A., Pace, A. B., et al. 2025b, arXiv e-prints, arXiv:2509.12313, doi: [10.48550/arXiv.2509.12313](https://doi.org/10.48550/arXiv.2509.12313)
- Tonry, J. L., Stubbs, C. W., Lykke, K. R., et al. 2012, ApJ, 750, 99, doi: [10.1088/0004-637X/750/2/99](https://doi.org/10.1088/0004-637X/750/2/99)
- Tsiane, K., Mau, S., Drlica-Wagner, A., et al. 2025, The Open Journal of Astrophysics, 8, 89, doi: [10.33232/001c.142072](https://doi.org/10.33232/001c.142072)

- van Albada, T. S., Bahcall, J. N., Begeman, K., & Sancisi, R. 1985, *ApJ*, 295, 305, doi: [10.1086/163375](https://doi.org/10.1086/163375)
- van der Marel, R. P., Fardal, M. A., Sohn, S. T., et al. 2019, *ApJ*, 872, 24, doi: [10.3847/1538-4357/ab001b](https://doi.org/10.3847/1538-4357/ab001b)
- Viel, M., Lesgourgues, J., Haehnelt, M. G., Matarrese, S., & Riotto, A. 2005, *PhRvD*, 71, 063534, doi: [10.1103/PhysRevD.71.063534](https://doi.org/10.1103/PhysRevD.71.063534)
- Virtanen, P., Gommers, R., Oliphant, T. E., et al. 2020, *Nature Methods*, 17, 261, doi: [10.1038/s41592-019-0686-2](https://doi.org/10.1038/s41592-019-0686-2)
- Vogel, C. M., & Abazajian, K. N. 2023, *PhRvD*, 108, 043520, doi: [10.1103/PhysRevD.108.043520](https://doi.org/10.1103/PhysRevD.108.043520)
- Wang, J., Frenk, C. S., Navarro, J. F., Gao, L., & Sawala, T. 2012, *MNRAS*, 424, 2715, doi: [10.1111/j.1365-2966.2012.21357.x](https://doi.org/10.1111/j.1365-2966.2012.21357.x)
- Wes McKinney. 2010, in *Proceedings of the 9th Python in Science Conference*, ed. Stéfan van der Walt & Jarrod Millman, 56 – 61, doi: [10.25080/Majora-92bf1922-00a](https://doi.org/10.25080/Majora-92bf1922-00a)
- Willman, B., Blanton, M. R., West, A. A., et al. 2005a, *AJ*, 129, 2692, doi: [10.1086/430214](https://doi.org/10.1086/430214)
- Willman, B., Dalcanton, J. J., Martinez-Delgado, D., et al. 2005b, *ApJL*, 626, L85, doi: [10.1086/431760](https://doi.org/10.1086/431760)
- Zhang, X., Chen, B., Chen, P., Sun, J., & Tian, Z. 2024, *MNRAS*, 528, 2653, doi: [10.1093/mnras/stae025](https://doi.org/10.1093/mnras/stae025)
- Zimmermann, T., Alvey, J., Marsh, D. J. E., Fairbairn, M., & Read, J. I. 2025, *PhRvL*, 134, 151001, doi: [10.1103/PhysRevLett.134.151001](https://doi.org/10.1103/PhysRevLett.134.151001)
- Zonca, A., Singer, L., Lenz, D., et al. 2019, *Journal of Open Source Software*, 4, 1298, doi: [10.21105/joss.01298](https://doi.org/10.21105/joss.01298)